Laser textured titanium surface characterization

Laura Convert, Eric Bourillot, Manuel François, Nicolas Pocholle, Florence Baras, Olivier Politano, Sophie Costil

Laser textured titanium surface characterization

Laura Convert[a*], Eric Bourillot[a], Manuel François[b], Nicolas Pocholle[a], Florence Baras[a], Olivier Politano[a], Sophie Costil[c]

[a] ICB UMR 6303, CNRS, Université Bourgogne Franche-Comté, UB, F-21078 Dijon, France

[b] LASMIS, Université de Technologie de Troyes, F-10004 Troyes, France

[c] ICB UMR 6303, CNRS, Université Bourgogne Franche-Comté, UTBM, F-90010 Belfort, France

*** Corresponding author:** Laura Convert

E-mail address: laura.convert@u-bourgogne.fr

Co-authors' e-mail addresses:

Eric Bourillot, eric.bourillot@u-bourgogne.fr

Manuel François, manuel.francois@utt.fr

Nicolas Pocholle, nicolas.pocholle@sayens.fr

Florence Baras, fbaras@u-bourgogne.fr

Olivier Politano, olivier.politano@u-bourgogne.fr

Sophie Costil, sophie.costil@utbm.fr

Keywords: pulsed nanosecond laser, topography, residual stress, XRD, scanning microwave microscopy SMM

Abstract

Laser surface texturing has emerged as an environmental technological option and fast developing technique to provide different surface conditions. In order to improve its efficiency, it is necessary to overcome the usual trial and error approach by carefully mastering operating parameters. The present work analyzes the effects of a pulsed nanosecond laser beam on the processing of titanium surfaces. The textured surfaces were characterized using various experimental techniques, including scanning microwave microscopy (SMM). The results show the impact of laser fluence, number of laser pulses and laser dimple pitch on textured surfaces mainly from a morphological (microscopies) and mechanical (XRD and SMM) perspective. The topography was analyzed according to the laser texturing parameters. A model of the cumulative effect of the number of laser pulses has been demonstrated. In addition, laser texturing modifies the surface residual stresses. Laser texturing effects on the surface mechanical state were analyzed by varying the laser texturing parameters and also by comparing isolated textured dimples and textured regions as a whole. Many changes were found such as surface topography and residual stresses, surface changes that need to be characterized and known to provide a better understanding of the performance and operating behavior of the materials.

1. Introduction

Laser processing technology has become a strategic part of surface engineering for many years. Laser material processing will continue to challenge conventional engineering processes, as laser technologies have already shown a definite interest due to their high precision, flexibility and productivity [1,2]. Indeed, laser surface treatments offer many benefits compared to other surface processes such as: (i) precision application, which allows precise treatments and modifications of surface properties on very small thicknesses (ii) multiplicity of techniques

(texturing, roughening, cleaning, shock hardening, etc.) leading to various tools for customizing the properties of surfaces, such as hardness, friction, fatigue and wear resistance (iii) no chemical effluents (iv) controlled deposited energy, providing a precise control of the heat input with minimal or no thermal effect on the underlying substrate [3]. Surface texturing is one of the most technologically appropriate laser surface treatment applications [4–7]. Over the last few decades, surface texturing has emerged as an attractive surface engineering option and has been used by researchers to generate micro/nanopatterns on operating surfaces. This technique allows creating simple or complex patterns on component surfaces according to their aesthetic or functional purposes and without altering bulk properties. In addition, this contactless process can be applied to hard-to-reach areas. Laser surface texturing has been used to improve the tribological performance of material interfaces [8–14]. More recently, laser surface texturing has also been applied to enhance adhesion of contact surfaces. Several authors have demonstrated the impact and benefits of textured surfaces to achieve optimal coating adhesion by analyzing interfacial resistance and evaluating coating-substrate adhesion [15–21]. A better fundamental understanding of laser-matter interaction is essential to precisely control the modification of materials at the nanoscale [22–29]. This way, some studies have investigated the surface modifications induced by laser treatment in terms of morphology, oxidation, hardening and thermal stresses [30–37]. The residual stresses induced by laser shock peening and present in femtosecond laser-induced periodic surface structures (LIPPS, ripples) were analyzed in [33,38–40]. In the present work, the laser texturing was conducted with a pulsed nanosecond laser. This type of laser treatment is very different from femtosecond laser texturing because of thermal effects. The present work focused on residual stresses induced by nanosecond laser texturing. Due to very localized changes, the final structural and mechanical state of the treated surface is difficult to highlight. However, the knowledge and control of these conditions are crucial to apply the treatment to industrial cases and thus propose new

developments. Indeed, the surface residual stresses have a direct impact on wear performance and fatigue life. In this study, a pulsed nanosecond laser was used to texture titanium surfaces. This work aims to improve the understanding of the laser texturing effects on surface topography, surface chemistry and mechanical state particularly using a new technique. Consequently, the effect of laser parameters (fluence, number of laser pulses, laser dimple pitch) on the evolution of surface states (morphology, residual stress, chemical composition) was analyzed. The surface topography and microstructure were assessed using optical microscopy, chromatic light confocal profilometry and scanning electron microscopy (SEM). The surface chemistry was characterized using X-ray photoelectron spectroscopy (XPS). Mechanical changes in the treated region were examined with two complementary techniques, which provide information at different scales: macroscopically via X-ray diffraction (XRD) and microscopically using a new technique under development: scanning microwave microscopy (SMM). Using X-ray diffraction, the global residual stress state near the surface at an average depth of a few micrometers (here 4 µm) was probed and averaged on a surface significantly larger than the grid step. The SMM technique was used to characterize the dimples and their environment because scanning microwave microscopy has extremely high spatial resolution and is suitable for more thorough lateral and depth analysis.

2. Materials and methods

2.1 Materials

The investigated substrate was made from commercially pure titanium “Ti ASTM Grade 2” (99% minimum titanium). Titanium cylinders with a diameter of 25 mm and a height of approximately 10 mm (from a bar) have been used for this work. Before laser texturing, all surfaces were mechanically polished and a chemical etching was applied (diluted Kroll etchant). Prior to laser treatments the titanium samples were carefully cleaned with acetone and dried.

2.2 Surface texturing

A pulsed Ytterbium-doped fiber laser (Quantel Ylia M20) operating at 1064 nm (near-infrared light) has been used to elaborate surface microstructures. It delivers short pulses of 100 ns. Depending on the pulse duration range, different beam-matter interaction mechanisms are predominant. For nanosecond laser pulses, the pulse length is much higher than the electron-phonon relaxation time of materials. In this case, the laser beam-matter interaction is considered as a thermal process. The successive stages involved are: (i) absorption of laser radiation (ii) surface heating (iii) evaporation and ejection of matter [25–29,31,32]. In this work, the laser spot was almost circular with a gaussian energy distribution. The theoretical effective diameter d_0 of the focused gaussian spot, calculated as

$$d_0 = \frac{4M^2\lambda f}{\pi D} \quad (1)$$

where d_0 is the beam diameter at the beam waist [m], M^2 the beam quality factor, λ the wavelength [m], f the focal length of the lens [m] and D the gaussian spot diameter at the lens [m], was found to be (59.4 ± 3.3) µm [41]. This diameter includes 86% of the beam energy and at the beads of which the focused intensity is down to $e^{-2} \cong 14\%$. The pulse repetition rate ν (or pulse frequency) could be adjusted from 20 to 100 kHz and the measured average power P_{avg} from 2.5 to 16.1 W. In this study, the energy flux delivered by the laser beam is characterized by the fluence. The fluence F of a laser pulse describes the optical energy delivered per unit area, in units of J.cm^{-2}. The fluence F is defined as

$$F = \frac{4P_{avg}}{\pi\nu {d_0}^2} \quad (2)$$

where P_{avg} is the average laser power [W], ν the pulse repetition rate [Hz] and d_0 the beam diameter [m]. Thereafter, the fluence is denoted Fx where x corresponds to the rounded value of the fluence in J.cm^{-2} (for example $F12$ means a fluence of 12 J.cm^{-2}). Similarly, the number

of laser pulses is denoted N*y* with *y* corresponding to the laser pulse number per dimple (for example N5 means 5 laser pulses per dimple). The incident laser beam was directed normal to the titanium target surface and focused by a lens with a focal length of 160 mm. All tests were performed in ambient air to create dimple textures. Such surfaces are usually used to improve the surface adhesion of coatings, it consists of individual small dimples arranged in a grid. Below the ablation threshold, the morphology of surfaces was not modified. Above the ablation threshold, dimples were produced. The central part of the irradiated area has been characterized by material removal, forming a crater, while material has been resolidified at the beads. The observed bead around the ablated crater has been formed due to the ejection of liquid molten metal by the recoil pressure and thermocapillary forces [42,43]. In this case, the grid size was 2 mm x 2 mm and the laser dimples were spaced with a pitch of 200 µm, 100 µm or 50 µm. Figure 1 shows an example of a textured surface and the characteristics of a dimple. The impact of laser fluence, number of laser pulses (i.e. the number of successive pulses in one place) and dimple pitch have been studied.

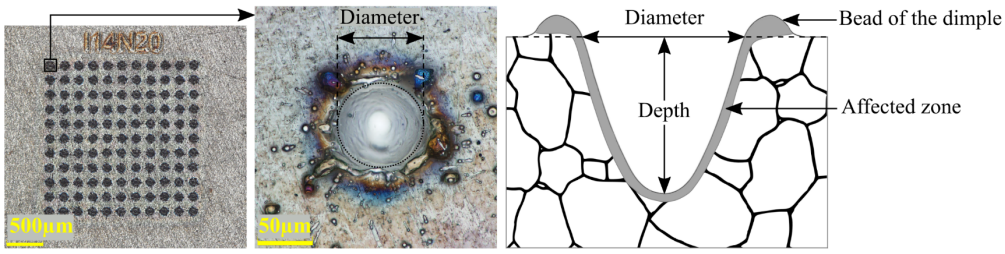

a) *b)* *c)*

Figure 1. Optical microscopy images of the treated surface (Ti ASTM Grade 2) – a) Texturing pattern obtained with a fluence of 11.6 J.cm^{-2}*, 20 pulses per dimple and a 200* µm *pitch; b) Zoom on one dimple in Figure 1a (the depth of the dimple is 29* µm *and its inside diameter is 76* µm*); c) Dimple characteristics*

2.3 Surface characterization

In order to investigate the topography of textured surfaces, morphological characterization was performed by means of optical microscope (Olympus DSX510) and chromatic light confocal profilometer (ALTIMET Altisurf© 500). The diameter and depth of dimples were then measured. The objective of the microscope is focused on the surface of the sample outside the dimple, and then the inside diameter of the dimple is defined at this focal plane. Each value presented is the average of three measurements with a standard deviation of 0.7 µm. The objective lens "MPLFLN50xBD" of the optical microscope with a 50x magnification was used to measure dimple parameters with a depth accuracy of ± 0.25 µm. The microstructure was imaged via scanning electron microscope (SEM Hitachi SU8230).

Due to the thermal effects of the laser treatment (in the case of pulsed nanosecond laser beams), localized oxidation phenomena can be expected particularly on metallic materials. To evaluate such modifications, the electronic structure of the studied surfaces was explored using X-ray photoelectron spectroscopy (XPS). The PHI 5000 VersaProbe spectrometer was employed in this study. Al Kα (1486.6 eV) was used as excitation source on the photoelectrons from the surface and the photoelectrons were collected through the energy analyzer. For each measurement, the average of 20 spectra was stored. CasaXPS software was then used for data processing (Version 2.3.24, www.casaxps.com, Teignmouth, United Kingdom) [44]. The adventitious carbon (C 1s) located at 284.8 eV has been used to calibrate the binding-energy scale.

3. Residual stress evaluation techniques: XRD and SMM

To investigate the residual stress state of the surfaces, X-ray diffraction (XRD) analysis were performed using the Bruker D8 Discover diffractometer. Tests were conducted using a copper anode (wavelength λ = 0.154184 nm). A collimator with 1 mm diameter was used. Thus, the

area irradiated by the X-ray beam covers at least 25, 100 and 400 dimples for the 200 µm, 100 µm and 50 µm pitches respectively. Measurements have been conducted on the {213} planes of the α phase at a 2θ angle of about 139°. Diffracted photons were collected with a 1D LynxExe XE^T detector. Eleven tilt angles ψ have been chosen between 0° and 60° with a 6° pitch. Stresses have been obtained using the so called $\sin^2\psi$ relation [45]. The X-ray Elasticity Constant (XEC) $\frac{1}{2}S_2^{hkl}$ was taken equal to 11.9 10^{-6} MPa^{-1}. The linear background noise evaluated on 30 points on each side of a peak has been subtracted. X-ray diffraction peaks were modelled using pseudo-voigt functions by considering $K\alpha_1$- $K\alpha_2$ doublet using Rachinger's assumptions [46]. As will be discussed later, the XRD technique used gives a global analysis of the stress state, i.e., it covers many dimples and thus provides an average value over the dimples and the unimpacted zone between dimples.

In order to analyze more locally the residual stresses in the surface, a scanning microwave microscope (SMM) was used. This innovative scanning probe microscope combines impedance measurement capabilities of a vector network analyzer (VNA) with the spatial resolution capabilities of an atomic force microscope (AFM) [47]. Agilent Technologies 5600LS AFM and Copper Mountain Technologies R180 VNA were used [48,49]. The conductive AFM tip is used as a local transmitter/receiver of microwaves to guide the microwaves field into material (Figure 2). The tip is always at a constant distance from the surface. Indeed, for each SMM measurement the AFM tip is in contact with the surface. The probe is a Rocky Mountain Nanotechnology platinum probe (model: 12PT400B) with a tip diameter of 20 nm, a spring constant of 0.3 $N.m^{-1}$ (± 40%) and a frequency of 4.5 kHz (± 30%) [50]. The VNA provides information about changes of impedance due to tip/sample interaction through the scattering parameters [51]. In this study, the parameter $S_{11} = \frac{\text{reflected signal}}{\text{incident signal}}$ has been analyzed.

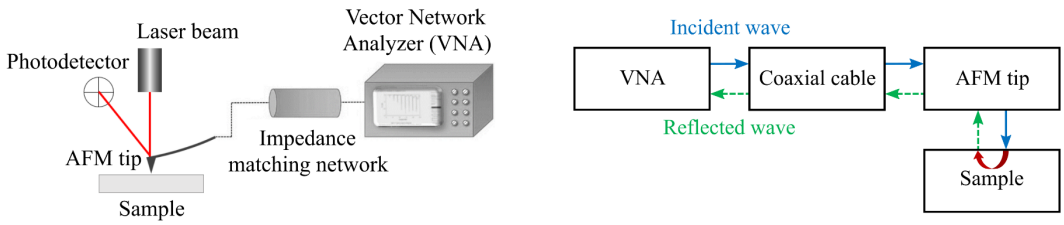

a) *b)*

Figure 2. Schematic diagrams of a scanning microwave microscope (SMM) – a) Architecture; b) Functional diagram

The used microscope was operated at microwave frequencies from 1 to 18 GHz.

In the case of metallic samples, the electromagnetic field can penetrate into the sample depending on the frequency used. The investigated depth corresponds to the skin depth and is defined as

$$\delta = \frac{1}{\sqrt{\pi \mu_0 \mu_r \sigma f}} \quad (3)$$

where δ is the skin depth [m], μ_0 the vacuum permeability ($4\pi\ 10^{-7}$ H.m^{-1}), μ_r the relative permeability of the conductor [H.m^{-1}], σ the electrical conductivity [S.m^{-1}] and f the frequency [Hz]. The electrical conductivity of titanium ASTM Grade 2 is $1.778\ 10^6$ S.m^{-1} and its relative permeability is 1.000 H.m^{-1} [52].

The electromagnetic wave of high frequency has a lower penetration compared to a low-frequency wave in a conductor. Skin depths were calculated for the different wave frequencies (Eq. (3)). In this study, the microwaves probed titanium surfaces with a depth ranging from 2.9 to 12.6 µm. The skin depth of metal defines the thickness of the layer where the wave field penetrating the metal fades out exponentially to zero.

The S_{11} coefficient is a complex quantity with a resistive and a reactive component. In the present paper, the magnitude of the real part has been explored since it is related to stresses through the piezo-resistive properties of the material. SMM measurement points followed a straight line passing through the center of three laser dimples spaced of 10 µm.

The measurement method and data processing are outlined below:

– Acquisition of the reference spectrum (Figure 3a): measurement of an untextured area

– Magnitude extraction at the resonance frequencies in the reference spectrum

– Acquisition of the sample spectrum (Figure 3a): measurement through a laser dimple

– Magnitude extraction at the resonance frequencies in the sample spectrum

– Determination of the difference between the sample resonance magnitudes and the reference resonance magnitudes (Figure 3b)

Recently, this non-destructive technique has been used to assess residual stresses induced by the shot-peening on metallic surfaces [53].

The magnitudes of the evaluated residual stresses are expressed in decibels [dB]. The correspondence between dB and MPa is a difficult issue that is beyond the scope of this paper.

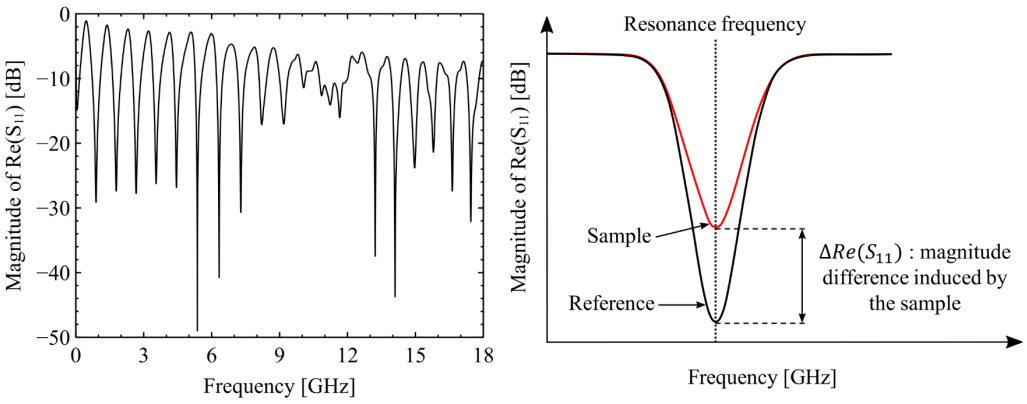

a) *b)*

Figure 3. Scanning microwave microscope (SMM) data processing – a) An example of frequency spectrum of the real part of reflection coefficient S_{11}*; b) Definition of the magnitude difference between the sample and the reference real parts of reflection coefficient* S_{11} *at a resonance frequency*

4. Results and discussion

4.1 Surface morphology

Prior to laser treatment, the surfaces were mechanically polished with the same procedure and chemically etched by Kroll's reagent during the same time. Thus the initial surfaces have a reproducible surface condition. The reference surface had an average surface roughness Sa (arithmetical mean height) of approximately 0.29 µm. Then, titanium samples were treated with a pulsed nanosecond fiber laser to produce microstructures with different input laser conditions. The structure morphology was varied using different laser parameters (fluence, number of pulses) and texturing parameters (pitch of dimples). Figure 4 shows texturing grids for a fluence of 11.6 J.cm^{-2} with 20 or 40 laser pulses and a pitch of 200 µm or 50 µm. For a 200 µm pitch, the dimples are clearly visible and evenly spaced (Figure 4a,c). Ejected material is accumulated at the periphery of the dimples (bead). Particles of material are present on the entire surface around the dimples and some are inside the craters. However, for a 50 µm pitch, the textured surface is very irregular and the dimples are not identifiable (Figure 4b,d). The structures formed are not periodic and are randomly intermingled. The pitch between the dimples significantly changes the topography of the textured surface. In order to analyze the effects induced by an isolated dimple and to evaluate the effects of their coupling, isolated dimples and grid dimples with a 200 µm pitch were studied. The coupling study is not possible for dimples with a 50 µm pitch.

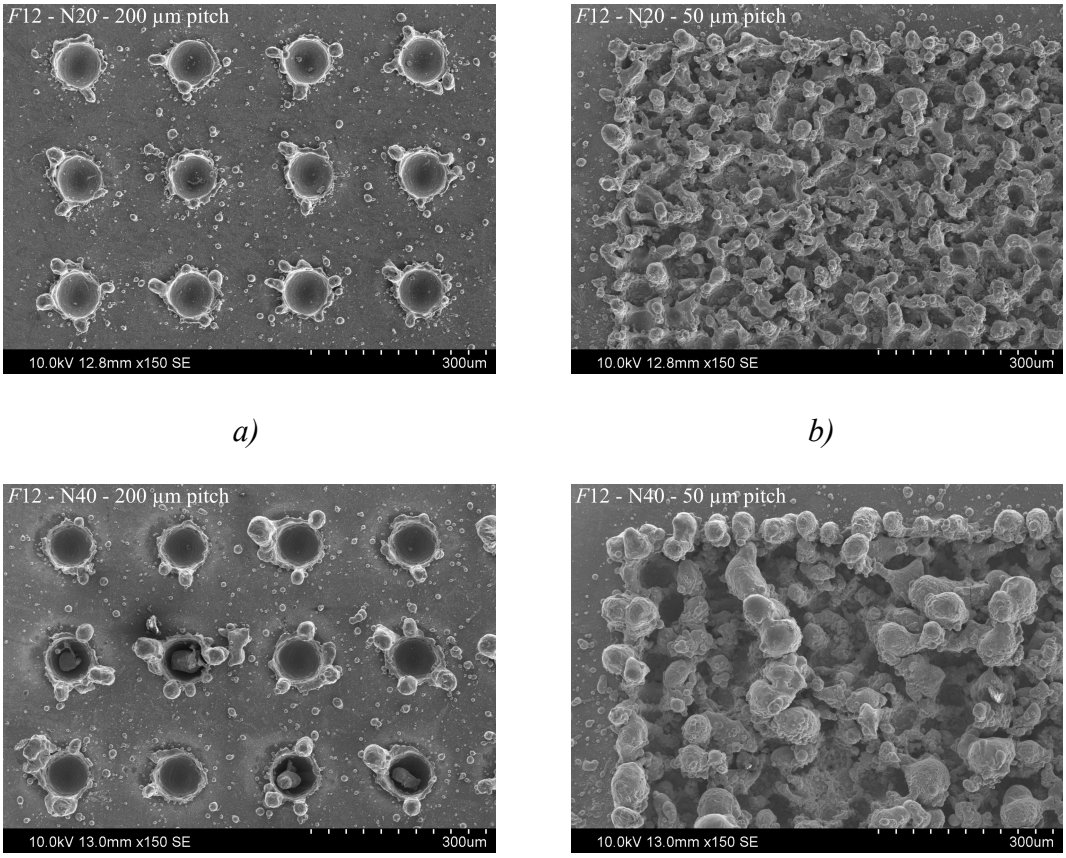

Figure 4. SE SEM images of titanium laser texturing grid areas obtained with a fluence of 11.6 J.cm^{-2} *– a) Dimples with 20 laser pulses and a pitch of 200* µm*; b) Dimples with 20 laser pulses and a pitch of 50* µm*; c) Dimples with 40 laser pulses and a pitch of 200* µm*; d) Dimples with 40 laser pulses and a pitch of 50* µm

In addition, by varying laser parameters, the effects of the number of laser pulses can be observed as illustrated in Figure 5; where optical microscopy images of dimples produced using a fixed laser fluence and a different number of laser pulses are shown. Nanosecond laser texturing has induced heat-affected zones. These areas can be easily detected by the noticeable colored ring around the dimple that corresponds to surface oxidation. The higher the number of laser pulses, the darker the color of the ejected particles. Thermal damage from the ablation zone is also identified in the target surface. Cross-sectional views of the dimples show a thin

zone, with altered microstructure, within the dimple with solidified metal at the dimple bead. The modified zone (finer microstructure) can be observed in Figure 6. This microstructural change is induced by the melting and resolidification of the metal. Its thickness is estimated at 3 µm for a dimple produced with a laser fluence of 11.6 J.cm^{-2} and 20 laser pulses. For the same fluence but a number of 40 laser pulses, the thickness of the modified microstructure zone is very close, about 3 µm. Different textures can be developed depending on the laser parameters, especially in terms of average dimple depth and diameter. Such variation in surface morphology can then be analyzed using profilometry as exposed in Figure 7. In addition, the dimple bead became more obvious with increasing laser fluence or laser pulse number. The higher the number of laser pulses, the more irregular the dimple bead (Figure 5 and Figure 7). The molten material is more and more important and is confined in the dimples. Under the pressure effect of the laser pulses, the material is ejected more violently towards the outside and irregular ejecta are produced on the surface due to the surface tension phenomena.

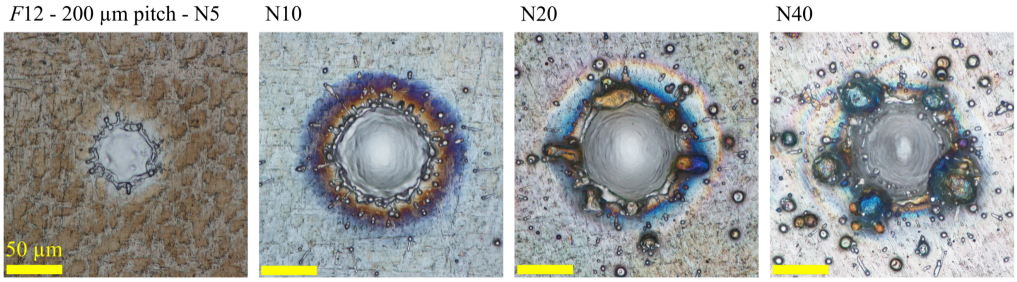

Figure 5. Optical microscopy images of titanium laser dimples obtained with a laser fluence of 11.6 J.cm^{-2} *and different number of pulses (5, 10, 20 and 40 pulses). Each dimple belongs to a dimple grid of 200* µm *pitch.*

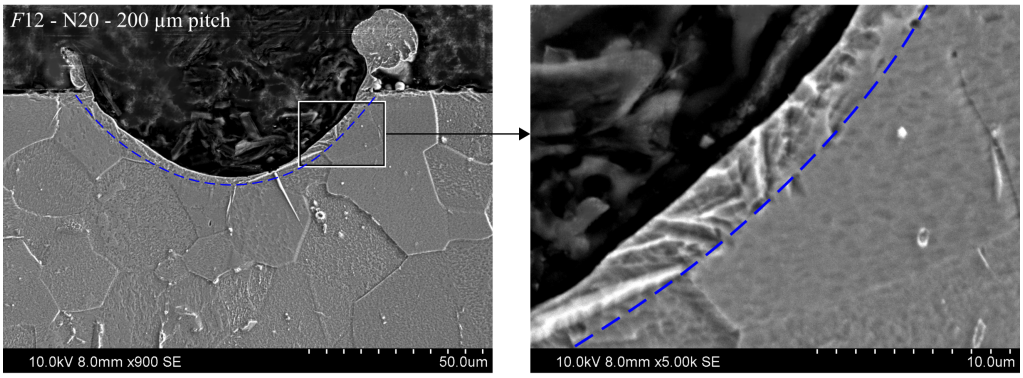

Figure 6. SE SEM cross-sectional image of a titanium laser dimple obtained with a laser fluence of 11.6 J.cm^{-2} *and 20 laser pulses. The dimple belongs to a dimple grid of 200* µm *pitch. The blue dotted line sets the zone with modified and finer microstructure.*

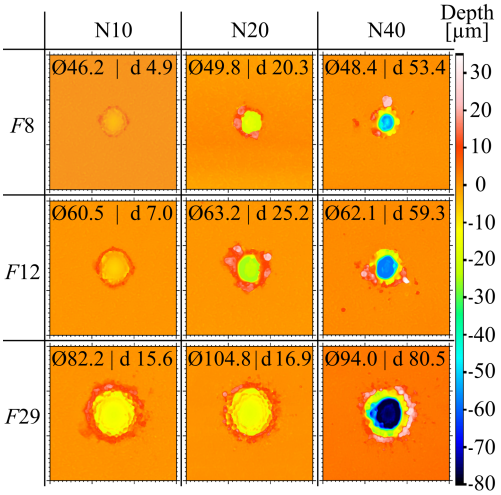

Figure 7. Profilometry images of isolated titanium laser dimples obtained with 3 different laser fluences (8.2 J.cm^{-2}*, 11.6* J.cm^{-2}*, 29.1* J.cm^{-2}*) and number of pulses (10, 20, 40). The color scale indicates the depth of the dimple. The size of the observation area is 300* µm x *300* µm*. The dimensions of the dimples (inside diameter Ø and dimple depth* d*) are given in* µm*.*

The graphs presented in Figure 8a,b and Figure 9 highlight the evolution of dimple depth and dimple diameter depending on the laser fluence and the number of laser pulses. The measured dimples belong to dimple grids with a 200 µm dimple pitch so that the topography of dimple can be analyzed without any interaction between the dimples.

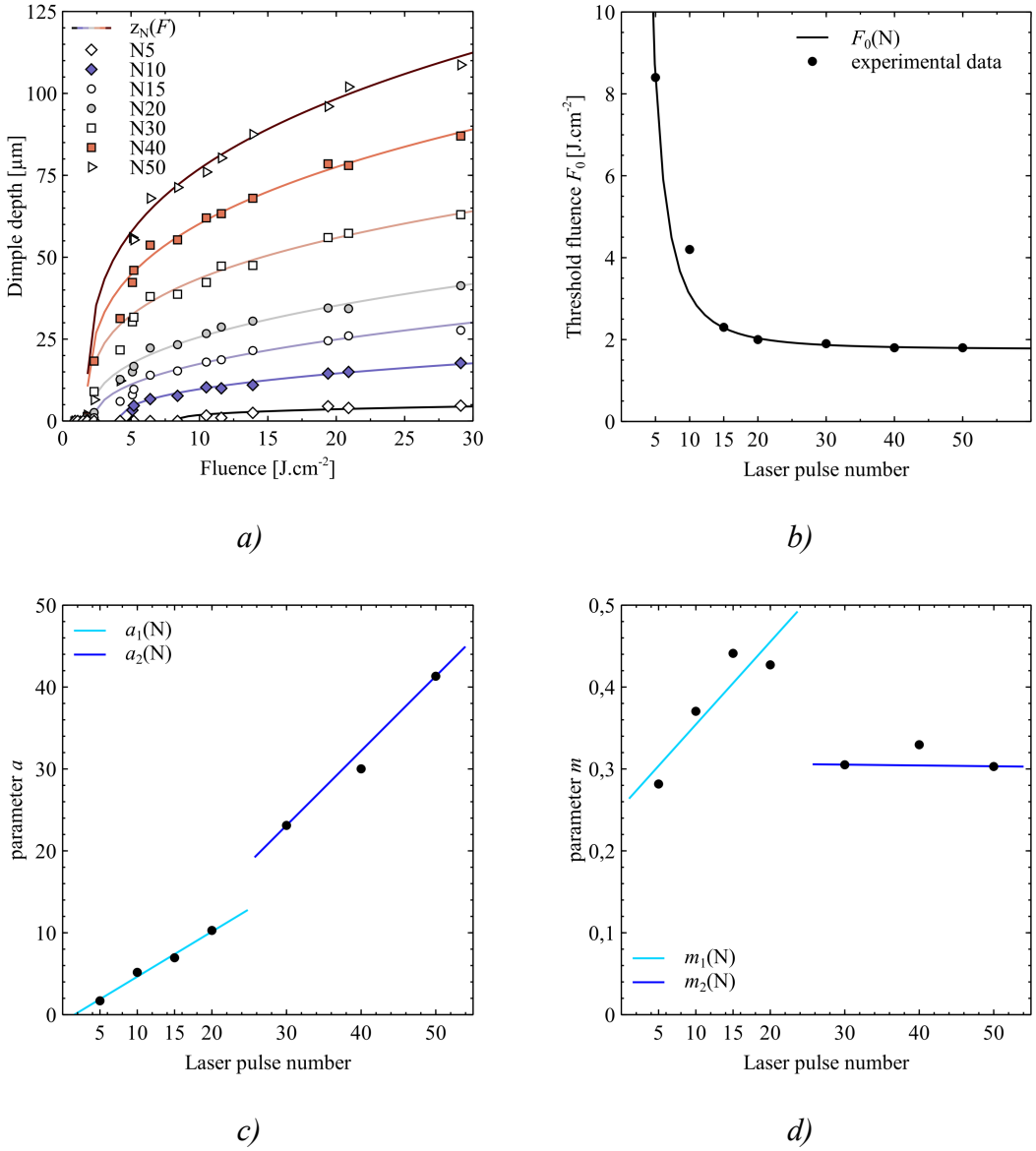

Figure 8. Depth evolution of titanium dimples belonging to 200 µm *pitch dimple grids generated by a pulsed nanosecond laser – a) Evolution of the dimple depth as a function of fluence for different numbers of pulses. The dots represent the measured values and the lines represent the fit with equation (4); b) Evolution of the threshold fluence as a function of number of pulses (dots: experimental data, line: fit with equation (5)* $F_0(N) = 1.76+273.94N^{-2.31}$*); c) and d) Evolution of the parameters a (*$a_1(N) = 0.55N-0.86$ *and* $a_2(N) = 0.91N-4.21$*) and m (*$m_1(N) = 0.0101N+0.2533$ and $m_2(N) = -0.0001N+0.3083$*) of equation (4) with the cumulative effect of the laser pulses. A regime change can be observed around 20 pulses.*

A threshold fluence can be observed below which the dimples have negligible depth. This threshold effect has already been observed in the literature [33]. Interestingly, this threshold is significantly higher for a low number of laser pulses and then saturates after about 20 pulses (Figure 8a). The dimple depth increases quickly above this threshold and then slows down. This can be explained by a purely geometric effect. As the aspect ratio of the dimple increases, i.e. when the depth increases, an increasing fraction of the molten and vaporized metal cannot leave the dimple and solidifies back on its walls. To describe the threshold effect and the slowing down of the depth z, a simple model is proposed:

$$z = a\,(F - F_0)^m \tag{4}$$

The fluence is denoted by F. The parameters a, F_0 and m are fitted by least squares regression for each series of laser treatment (at a fixed pulse number). In this equation, the increase of depth with the number of laser pulses does not appear explicitly. Thus, following the work of Jee et al. [33], a cumulative model of the effect of the number N of laser pulses is proposed:

$$F_0 = A + B\ \mathrm{N}^p \tag{5}$$

where F_0 is the threshold fluence, A, B and p are fitted constants. The fit of this model can be seen in Figure 8b. Several differences between this model and the model proposed by Jee et al. can be highlighted. Here, a constant term A is introduced to take into account the fact that, when the fluence is too low, the heat deposited in the material dissipates between two laser pulses. Below a threshold fluence, there is no ablation whatever the number of laser pulses (Figure 8b). This term does not appear in the study of Jee et al. because they observe surface damage of copper or aluminum with no or limited ablation effects. The results presented here show that below 2 J.cm^{-2} only ripples or flat melting can occur and the metal is not ejected by the laser beam. The value of exponent p is also very different, −2.31 in this study and −0.08 in the Jee et al.'s study. This can be explained by the difference in thermal conductivity which is high for

copper or aluminum and medium for titanium. Figure 8b shows that, for a low number of laser pulses (< 5), a very high fluence is required to start the ablation, so the cumulative effect of the laser pulses is very important to achieve an efficient surface texturing. However, it can also be seen that this cumulative effect quickly saturates after 20 laser pulses. This could be interpreted by the appearance of a thermal equilibrium state after 20 pulses. This regime shift around 20 pulses can also be observed as the parameters a and m of equation (4) evolve with the number of laser pulses (Figure 8c and Figure 8d).

The evolution of the dimple diameter with the fluence and the number of pulses can be observed in Figure 9. It can be clearly seen that, except for the 5 pulse series, there is no cumulative effect of the number of pulses. This means that the dimple diameter is mainly controlled by the laser beam diameter. The increase in dimple diameter with fluence can be attributed to the Gaussian profile in the beam cross section. As fluence increases, the central part of the beam, where the intensity is above an ablation threshold, increases in diameter and represents a larger fraction of the beam cross section.

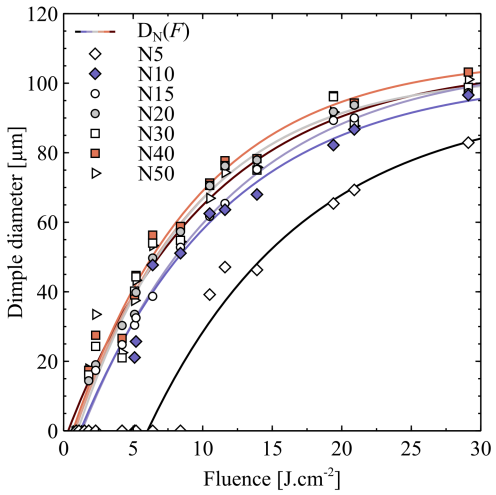

Figure 9. Evolution of the dimple diameter as a function of laser fluence for different numbers of laser pulses. The lines are exponential laws as $D_N(F) = k_1 - k_2\, e^{qF}$ *(k_1, k_2 and q are constants). Titanium dimples belong to 200* µm *pitch dimple grids generated by a pulsed nanosecond laser.*

The evolution of volume as a function of fluence and number of pulses can also be analyzed. The volume is computed from the radius r and depth z of the dimples assuming that they have the shape of a cone $V = \pi r^2 z/3$. Other assumptions (paraboloid, cylinder, etc.) would not affect the conclusions. It was found that, above a fluence threshold F_1 and a pulses number threshold N_1, the dimple volume evolves linearly with laser fluence F (for constant N) and linearly with laser pulse number N (for constant F), following equation (6):

$$V = b(\mathrm{N} - \mathrm{N}_1)(F - F_1) \qquad (6)$$

This evolution is represented in Figure 10a.

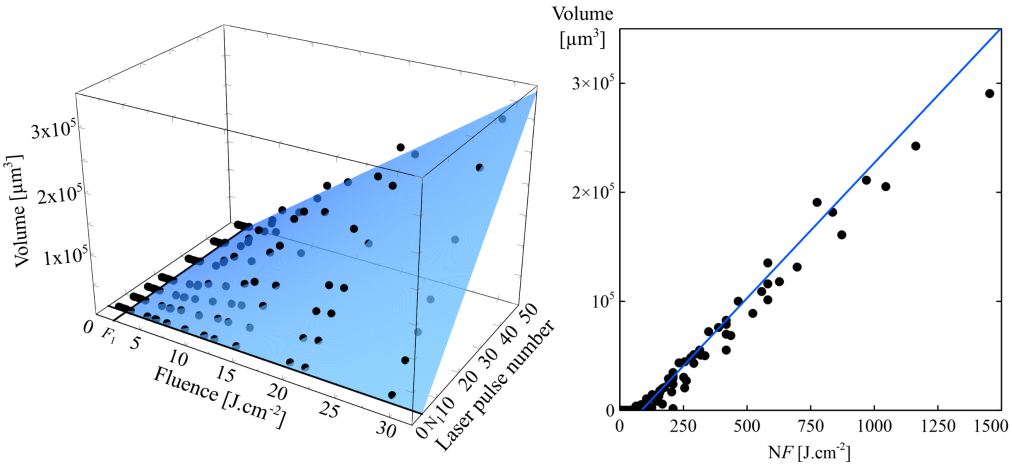

a) *b)*

Figure 10. Evolution of dimple volume (ablated volume) – a) Evolution of the dimple volume as a function of fluence and number of pulses. The blue surface is the least square fitting of equation (6) to the experimental points (black dots). The black lines represent the fitted thresholds F_1 and N_1; b) Evolution of the ablated volume versus total deposited energy density NF. The slope of the blue line is equal to the coefficient b of equation (6) fitted on the triplets (N, F, V).

Indeed, it can be observed in Figure 10b that, when all the experimental volume values are plotted versus the total deposited energy density, i.e., the product of fluence and the number of pulses, they tend to follow a straight line. As a result, the terms $\mathrm{N}F_1$ and N_1F in equation (6) have a very limited effect on the evolution of the ablated volume and beyond a threshold the dimple volume is proportional to the energy density. However, this proportionality does not describe all the details of the experiments. The straight line in Figure 10b has a slope b. This coefficient was obtained by fitting equation (6) to all experimental triplets (N, F, V). At high fluence, the black dots are located below the straight line. This can be explained by geometrical effects: when the dimples are deeper, a fraction of the molten/evaporated material is not ejected or redeposited in the dimple.

The surface colors reflect chemical changes, so XPS analysis were performed to identify the chemical transformations induced by laser treatment.

4.2 Chemical analysis

In addition to the morphology, chemical studies by XPS were completed to investigate the chemical effect of laser treatment. XPS measurements were carried out on the outstanding features of the dimples, namely the bottom and the bead. The dimples were produced with a laser fluence of 11.6 J.cm^{-2} or 29.1 J.cm^{-2}, and 10 or 15 laser pulses. The chemical composition of studied areas has been quantified and presented in Figure 11. Carbon and calcium were considered as contamination and not as products of laser processing of titanium surfaces. The oxygen content of the untextured area is relatively high. Besides the samples were stored in ambient air and temperature conditions for six months. They were thus affected by natural surface oxidation. At the beads of the dimples, the oxygen content increases significantly when increasing the laser fluence and slightly when increasing the number of laser pulses. At the bottom of the dimples, a significant percentage of nitrogen is measured. The presence of

nitrogen increases for both laser fluence and number of laser pulses. As demonstrated in Figure 11, the increase in oxygen can be linked to the formation of titanium dioxide (TiO_2) as well as the increase in nitrogen to the formation of titanium nitride (TiN). Indeed, high resolution spectra in the energy range of the Ti 2p signal obtained at different regions on a textured titanium surface (untextured area, bottom of dimple, bead of dimple) have highlighted the formation of these elements. When the raw data have been fitted with several chemical states (TiO_2, TiN and Ti metal), several results were found:

– the untextured area is predominantly composed of titanium dioxide,

– the beads of the dimples consist essentially of titanium dioxide,

– the bottom of the dimples are essentially composed of titanium nitride and titanium in metallic form.

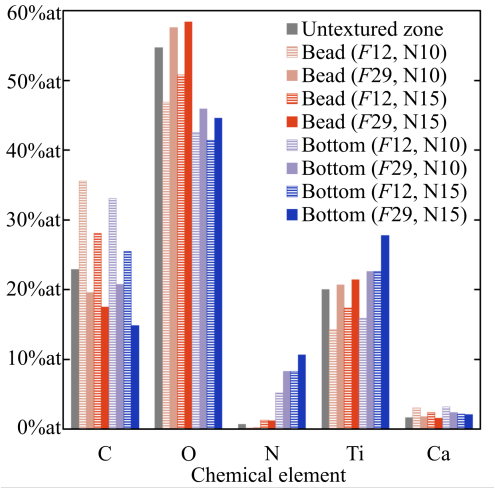

Figure 11. Chemical composition of areas at the bottom and at the bead of laser textured dimples with a laser fluence of 11.6 J.cm^{-2} *or 29.1* J.cm^{-2}*, and 10 or 15 laser pulses (composition expressed in atomic percentage)*

These Oxides and nitrides formed due to the presence of ambient air will alter the surface chemistry and potentially the reactivity and adhesion of a coating or the outcome of subsequent

treatments. If these surface chemical species prove problematic, laser treatments could be conducted under argon or under a primary vacuum.

4.3 Residual stress evaluation

Laser treatment causes an increase in temperature, melting and evaporation of the metal. The question arises whether the surface has undergone any mechanical changes. However, residual stresses affect surface integrity, cracking, adhesion of coatings; hence, the mechanical properties of laser textured surfaces have to be studied. In order to assess residual stresses, the textured areas (areas 2 mm x 2 mm) were analyzed macroscopically using XRD and locally via SMM. Isolated dimples were also investigated by SMM only. XRD measurements allow an assessment of the global residual stresses of textured titanium surfaces. Indeed, the average penetration depth of X-rays was 4.15 µm and the analyzed surface was a spot of 1 mm in diameter. Thus, the X-ray measurements provide an average of the residual stresses both inside and outside the dimples. By contrast, the scanning microwave microscopy collects local information over a depth range.

Firstly, XRD tests were conducted on textured surfaces. The impact of the dimple pitch was studied and hence the residual stresses were measured for texturing grids with a pitch of 200 µm and 50 µm. As illustrated in Figure 12a, the level of residual stresses is higher for a 50 µm pitch than a 200 µm pitch.

Indeed, the surface textured with a dimple pitch of 50 µm shows residual stresses about 15 times higher than the one textured with a 200 µm pitch. In the case of a 50 µm pitch, the effects of the laser pulses appear to overlap with each other and result in a very irregular and extremely rough surface (Figure 4b,d). As a result, XRD measurements at fluences higher than 10 J.cm^{-2} or 40 laser pulses could not be performed because the diffraction peaks were too broad and distorted. For surfaces textured with 10 and 20 laser pulses, the residual stresses increase

gradually with laser fluence (Figure 12a). For surfaces textured with 40 laser pulses, residual stresses increase quickly with laser fluence and appear to decrease when the fluence is 29.1 J.cm^{-2} (Figure 12a). In particular, the effect of the laser pulse number, for a laser fluence of 11.6 J.cm^{-2}, is shown in Figure 12b. Although the untextured surface was not measured, the residual stresses of textured titanium surfaces increase with the number of laser pulses. Laser treatment introduced tensile stresses and the dimpled surface with a pitch of 200 µm is in tension above 20 laser pulses.

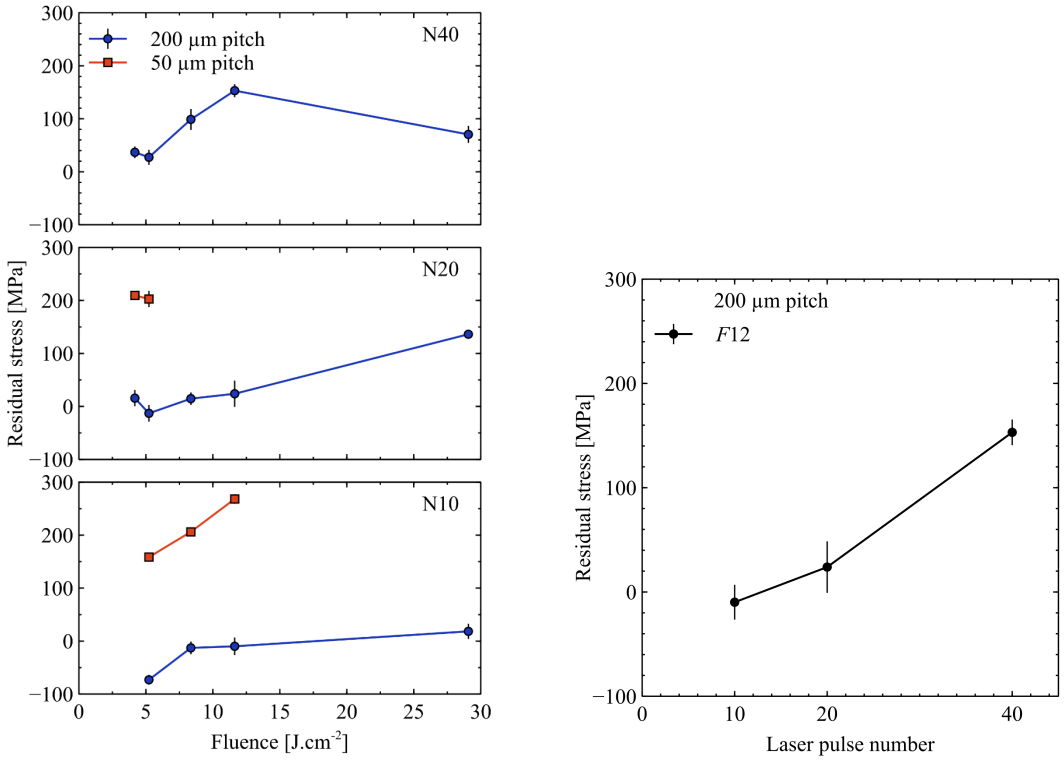

a) *b)*

Figure 12. Residual stresses of textured titanium surfaces measured via XRD using CuKα radiation – a) Effect of laser fluence, number of laser pulses and dimple pitch on residual stresses; b) Evolution of residual stresses as a function of number of laser pulses, for dimples produced with a laser fluence of 11.6 J.cm^{-2} *and a dimple pitch of 200* µm.

In addition, isolated dimples and four successive dimples of a textured area produced with a laser fluence of 11.6 J.cm^{-2} were analyzed via SMM and compared. The objective is to study whether the residual stresses are the same for an isolated dimple or for a periodic arrangement of dimples in order to characterize the textured surface condition. Only SMM can allow this comparison given the limited dimensions of an isolated dimple. Analysis of the S_{11} parameter highlighted a modification of the residual stress state. The impact of the number of laser pulses was studied by comparing dimples produced with 20 laser pulses and 40 laser pulses. Figure 13 and Figure 14 reveal the residual stress profiles for isolated dimples or dimples from a grid of dimples, produced with the same fluence and 20 or 40 laser pulses. The measurements conducted on the untextured surface were subtracted from the set of measurements carried out on the textured surface (Figure 3). Thus, the baseline at 0 dB represents the reference level, corresponding to the level of initial residual stresses present in an untextured surface. A positive (resp. negative) value of the signal corresponds to a tensile (resp. compressive) stress state. The type of residual stresses depends on the position of the AFM tip in relation to the laser dimples and also on the probed depth depending on the analysis frequency. Indeed, alternating compressive and tensile residual stresses can be observed below the dimples. The very superficial surface tension can be explained by the thermal effects of laser treatment. Below the surface, the compressed material attempts to regain its original volume, creating compressive stresses. The compressive residual stresses observed at greater depths could be due to the above phenomenon or to the overall residual stress balance. In addition, the isolated dimples produced with 40 laser pulses show a wider stress profile than the isolated dimples produced with 20 laser pulses (Figure 13). The variation in magnitude is similar for both different isolated dimples. For isolated dimples, the number of laser pulses induced a widening of the residual stress area but did not affect the residual stress magnitude level. The residual stress-affected zone, by spatial extrapolation, has a diameter of 100 µm for the isolated dimples produced with 20 laser

pulses and a diameter of 200 µm for those obtained with 40 laser pulses. This residual stress state revealed via SMM is quite independent of the dimple shape. Indeed, the dimple diameter size with 20 and 40 pulses (Figure 7) is similar while the SMM results are different (Figure 13). In addition, increasing the number of laser pulses affects the residual stresses near the bead (Figure 13b). Textured surfaces with a dimple pitch of 200 µm were analyzed.

As it appears in Figure 14a, each dimple of 200 µm pitch produced with 20 pulses presents an equivalent magnitude. For these dimples, the variation ranges are very close and the area between the dimples appears to be free of additional residual stresses. Thus, under these texturing conditions, the residual stresses of a dimple are not influenced by the formation of adjacent dimples. Adjacent dimples are the neighboring dimples near the studied dimple. In Figure 15a, it can be observed that the first dimple has three adjacent dimples (blue hatched dimples), while the second, third and fourth dimples have five adjacent dimples (red gridded dimples for the fourth dimple). By contrast, the magnitude recorded for successive dimples of 40 laser pulses is very different as it can be observed in Figure 14b. The higher the number of pulses, the higher the residual stress levels. For 40 pulses, the residual stress level between dimples is significant. In addition, as previously shown for isolated dimples produced with 40 laser pulses, the residual stresses extend at least 100 µm on either side of the center of an isolated dimple. Thus, for a grid of dimples with a 200 µm pitch, the residual stresses on the surface are impacted by the formation of adjacent dimples.

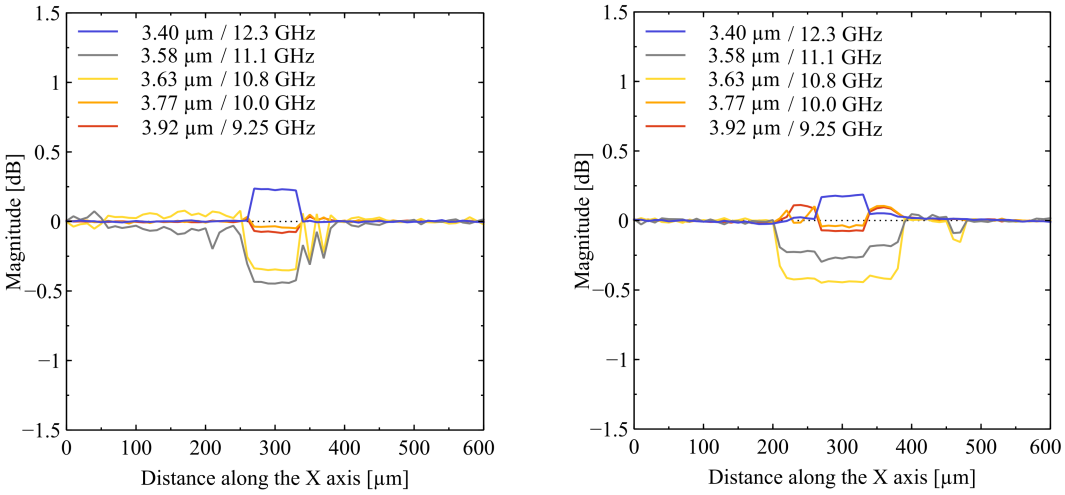

a) *b)*

Figure 13. S_{11} *magnitude evolution through an isolated textured titanium dimple with a laser fluence of 11.6* J.cm^{-2}*, along the X axis for five penetration depths. SMM measurements were conducted along the X axis passing through an isolated textured dimple – a) The laser fluence is 11.6* J.cm^{-2} *and the pulse number is 20; b) The laser fluence is 11.6* J.cm^{-2} *and the pulse number is 40*

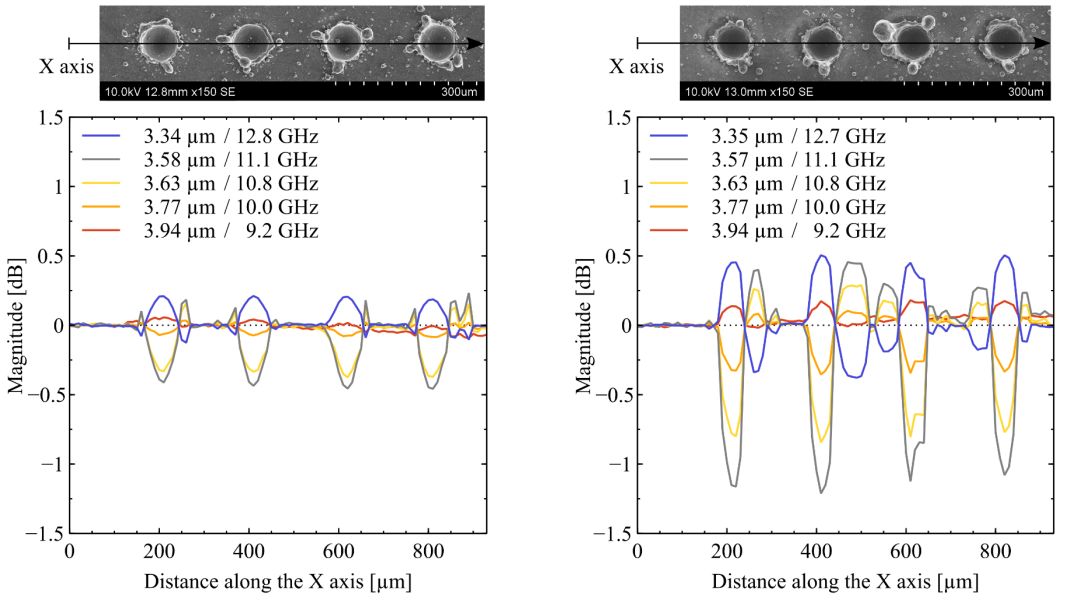

a) *b)*

Figure 14. S_{11} *magnitude evolution through successive textured titanium dimples with a laser fluence of 11.6* J.cm^{-2}*, along the X axis for five penetration depths. SMM measurements were*

performed through four successive grid dimples along the X axis, as shown in the SEM images – a) The laser fluence is 11.6 J.cm^{-2} *and the pulse number is 20; b) The laser fluence is 11.6* J.cm^{-2} *and the pulse number is 40*

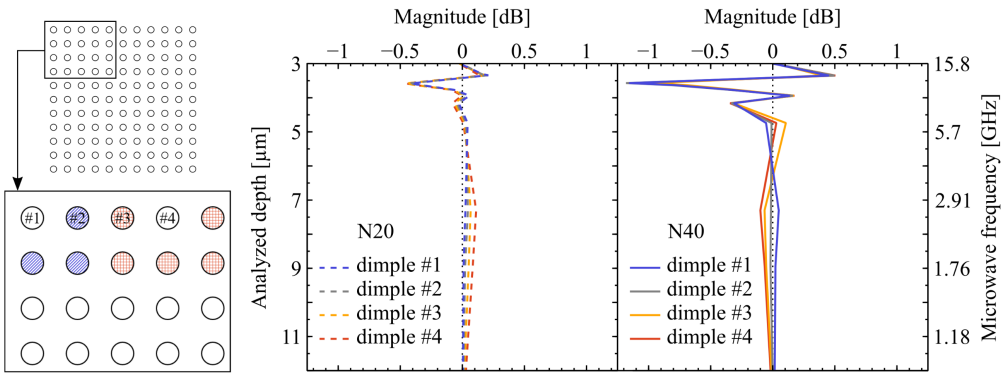

a) *b)* *c)*

Figure 15. a) Identification of adjacent dimples for dimple #1 (blue hatched dimples) and for dimple #4 (red gridded dimples) from a dimple grid with a 200 µm *pitch; b) Evolution of the* S_{11} *magnitude difference in the bottom depth of the four successive dimples from dimple grids with a 200* µm *pitch, dimples produced with 20 laser pulses; c) Dimples produced with 40 laser pulses*

Figure 15b,c and Figure 16 show the evolution of the residual stresses below the bottom (from 3 to 12 µm) of successive dimples produced with 20 and 40 pulses. For 20 laser pulses, the residual stress profile is almost similar regardless of the dimple (Figure 15b). However, for 40 laser pulses, a stabilization of the residual stress profile is observed from dimple #3 (Figure 15c). Figure 15c clearly illustrates the impact of adjacent dimples, especially their cumulative effect on residual stresses. The adjacent dimples also changed the depth stress state. In order to study the impact of the number of laser pulses on the residual stresses below the bottom of the dimples, with less impact from adjacent dimples, the residual stress profiles of dimple #1 were compared and presented in Figure 16. From 3 to 4.5 µm below the bottom of

the dimple, the magnitude variations are higher for 40 pulses than for 20 pulses. The residual stresses below 7.5 µm, from the bottom of the dimples, become smaller and smaller and tend to zero.

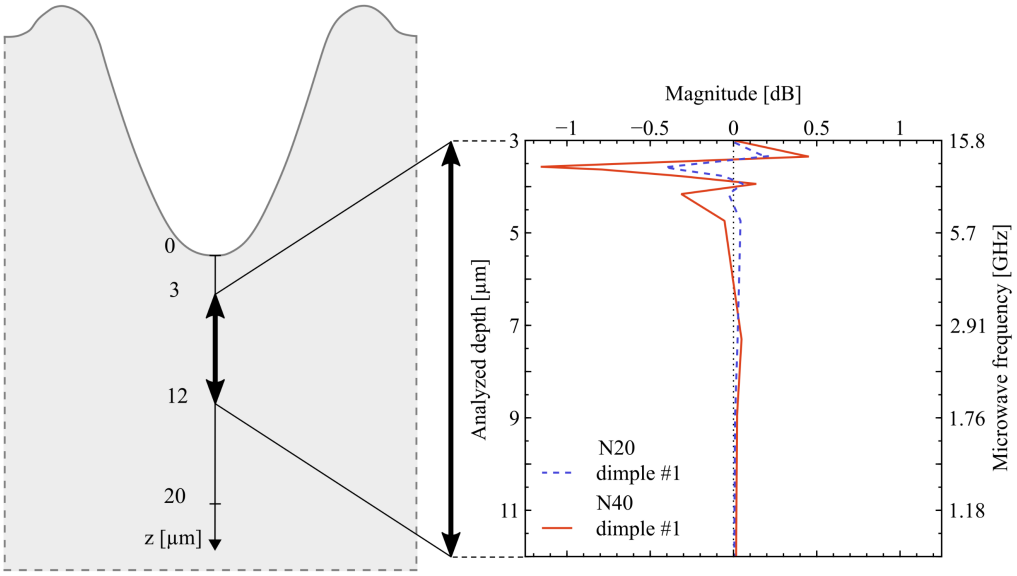

Figure 16. Evolution of the S_{11} *magnitude difference below the bottom of the dimples #1, produced by a laser fluence of 11.6* $J.cm^{-2}$ *with 20 or 40 laser pulses*

Figure 17 compares the depth residual stress profiles obtained at the bottom of isolated dimples and grid dimples #1 produced with 20 or 40 laser pulses. For 20 laser pulses, the SMM signal magnitudes of isolated and grid dimples are similar. However, a slight shift in residual stresses towards 3.6 - 3.7 µm is observed when comparing the profiles at the bottom of isolated dimples produced with 20 and 40 laser pulses. Thus, increasing the number of laser pulses leads to a change in the depth residual stress profile as well as a change in the residual stress level in the area between the dimples. For 40 laser pulses, the residual stress profile at the bottom of a grid dimple is significantly altered compared to the profile observed at the bottom of an isolated dimple. Hence, dimple creation with 20 laser pulses shows individual residual stress behavior even for dimple grids. By contrast, for dimple grids produced with 40 laser pulses, dimple

creation has a matrix behavior. Indeed, although dimple #1 has few adjacent dimples, Figure 17 highlights that the residual stresses at the bottom of dimples produced with 40 laser pulses were affected by the formation of adjacent dimples (cumulative effects).

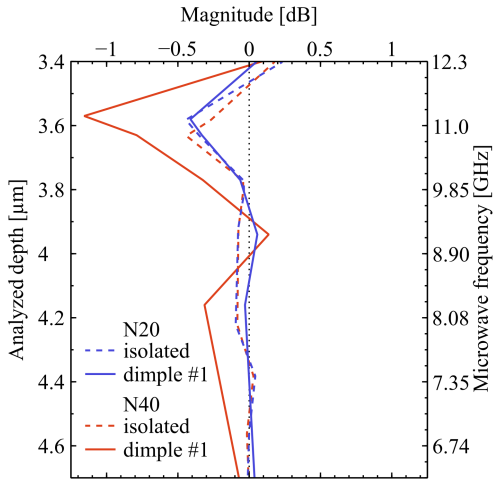

Figure 17. Evolution of the S_{11} *magnitude difference below the bottom of the isolated dimples and dimples #1, produced by a laser fluence of 11.6* $J.cm^{-2}$ *with 20 or 40 laser pulses*

SMM provides a local measurement of residual stress while XRD delivers an average residual stress of a larger region. In (x, y) the size of the probed volume is in the micrometer range for XRD and in ten nanometers for SMM. In depth, the signal propagates at a finite average penetration depth characterized by the skin depth. As the penetration depths are comparable, the two techniques differ essentially in the spot size. Hence, they are complementary, XRD providing a global analysis of the affected area and SMM a local analysis.

Averages of the SMM measurements from 3 to 3.9 µm were calculated and are plotted in Figure 18. Dimples #3 and #4 are studied because they have more adjacent dimples. As a result, they are more characteristic of laser texturing effects. The area between the dimples is more in compression for 20 pulses and more in tension for 40 pulses compared to the untextured surface. However, compressive residual stresses at the bottom of the dimples are noted, potentially due

to residual stress balancing. If the measurement line is generalized to a surface, the majority of residual stresses should be in compression for 20 laser pulses and in tension for 40 laser pulses. Indeed, the area of the dimples is relatively small compared to the area between the dimples. Increasing the number of laser pulses potentially leads to the development of tensile residual stresses. The data in Figure 12a reveal that the residual stresses measured using XRD increase with the number of laser pulses. Both methods, XRD and SMM, lead to the same observation regarding laser texturing: increasing the number of laser pulses generates a tensile residual stress in the surface. The presence of tensile residual stresses can be explained by the mechanisms involved during resolidification and cooling of the metal. During solidification and cooling, the liquid material contracts. However, the cold material around the molten zone prevents this contraction, thus generating tensile residual stresses in the surface.

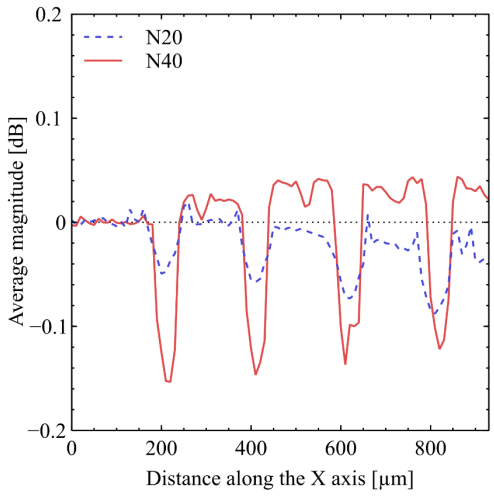

Figure 18. Evolution of the average magnitude between 3 µm *and 3.9* µm *depth for successive dimples produced with a laser fluence of 11.6* J.cm^{-2} *and 20 or 40 laser pulses*

A grid of dimples produced with a laser fluence of 10.5 J.cm^{-2} and 10 laser pulses was measured via XRD. Using scanning microwave microscopy, as shown in Figure 13a, the residual stresses induced by a laser treatment of fluence 11.6 J.cm^{-2} and 20 laser pulses extend in (x, y) over

50 µm on either side of the dimple center. For the current sample, it can be assumed that the dimples have little or no effect on the stress profile of the area between the dimples. The residual stress of the area between the dimples is assumed to be equal to the residual stress of the untextured surface. With this assumption and assuming that the stresses are homogeneous within the dimples, a simple computational model was defined to estimate the average residual stresses of the dimples (denoted σ_D) and between the dimples (denoted σ_B). In this case, the measured residual stress (denoted σ_M) via XRD is the area average of the two stresses. The area of a dimple and the area between dimples are displayed in Figure 19.

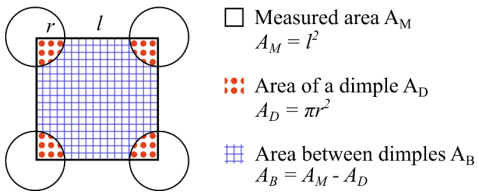

Figure 19. Definition of the area of a dimple and the area between dimples. The measured area is averaged to a square of length l, where l is the dimple pitch. The radius r is the average outer diameter of the dimples (cavity and bead).

The measured stress is expressed as

$$\sigma_M = X_D\sigma_D + X_B\sigma_B \quad (7)$$

where $X_D = \frac{A_D}{A_M}$ is the proportion of the area of a dimple to the measured area, $X_B = \frac{A_B}{A_M} = 1 - X_D$ the proportion of the area between the dimples to the measured area, σ_M the measured residual stress, σ_D the average residual stress of a dimple and σ_B the average residual stress of the area between the dimples (in this work assumed to be equal to the residual stress of the untextured surface). According to this model, the average residual stress induced by laser treatment is concentrated in the dimples. The studied dimples have a pitch of 200 µm,

an inside diameter of 60 µm and an outside diameter of 90 µm. The equation (7) is used to calculate the average residual stress of a dimple as

$$\sigma_D = \frac{\sigma_M - (1 - X_D)\sigma_B}{X_D}$$

where σ_M = (−78.4 ±13.7) MPa, σ_B = (−144.6 ±11.4) MPa and $X_D = \frac{81\pi}{1600} \cong 0.159$

Then the average residual stress of a dimple can be estimated to σ_D = 271.6 ±25.9 MPa. In conclusion, dimple texturing with a pulsed nanosecond laser induces tensile residual stresses in the surface of about 4 – 5 µm depth. The presence of these overall tensile residual stresses at the surface and localized compressive residual stresses at the bottom of the dimples induced by the laser treatment is important to know. This surface stress state should be taken into account when selecting additional treatments (e.g. coatings) and for the lifetime of the material. The presence of tensile residual stresses in the surface is detrimental to the performance of the surfaces. As the surface residual stresses can be assessed microscopically and macroscopically, optimal laser processing conditions could be searched by modifying the fluence, the number of laser pulses and the dimple pitch in order to prevent damage to the surface mechanical properties during laser texturing. Post-treatment can also then be considered to relax the stress state on the surface or to introduce compressive residual stresses, such as cavitation peening or laser shock peening techniques to improve the mechanical properties of the textured surfaces.

5. Conclusions

The experimental results presented in this paper confirm that laser texturing has significant effects on the surface layers of metallic materials. Microanalysis highlighted that the depth of the dimples increases with increasing laser fluence or number of laser pulses. The diameter of the dimples increased with increasing laser fluence and showed an asymptotic behavior with increasing number of laser pulses. A threshold ablation fluence is observed which is significantly higher for a low laser pulse number and then saturates after about 20 pulses. A

cumulative model of the effect of laser pulse number N on dimple depth was presented. The ablated volume was also analyzed. Above a fluence threshold and a pulse number threshold, the dimple volume evolves linearly with the laser fluence (for a constant pulse number) and linearly with the laser pulse number (for a constant fluence). These thresholds were interpreted as a consequence of thermal effects. In addition, the laser treatment involved the formation of titanium dioxide on the surface of the beads and the formation of titanium nitride at the bottom of the dimples. From a mechanical perspective, residual stress analysis showed that laser texturing created overall tension. Indeed, the impact of the number of laser pulses and the dimple pitch was investigated using XRD and SMM analysis. Locally, SMM measurements revealed that the stress profile of isolated dimples produced with 40 laser pulses was greater than for isolated dimples produced with 20 laser pulses. Thus, by increasing the number of laser pulses, the mechanical state of the adjacent area is more affected. And the textured surfaces exhibited tensile residual stresses in the surface between the dimples and compressive residual stresses at the bottom of the dimples. In addition, XRD studies of the effect of dimple pitch revealed that decreasing the pitch generated a significant increase in the average residual stress. SMM measurements do not currently provide a quantitative estimate but give valuable results on surface and depth residual stresses with excellent spatial resolution. A study is underway to determine the exact correspondence between the residual stresses measured using XRD and SMM. Numerical simulation plays a very important role in predicting the mechanical behavior of parts. The simulation provides a better understanding of the impact of laser treatment on the occurrence of residual stresses and defect formation. Atomic scale molecular dynamics or finite element approaches could be undertaken to analyze or quantify residual stresses.

Acknowledgements

This work was supported by the Bourgogne Franche-Comté region, the French Technological Research Institute for Materials, Metallurgy and Processes (IRT M2P), the French program Plan d'Investissement d'Avenir (PIA) and the French National Research Agency (ANR) through the OmicroN project (Grant No. ANR-19-CE42-0007) and the EUR-EIPHI Graduate School (Grant No. ANR-17-EURE-0002). Thanks are expressed to Youness El Moudden and Léa Le Joncour who provided some data for this paper.

REFERENCES

[1] J. Lu, Traitements de surface mécaniques – Effets sur les matériaux, Traitements des métaux. (2015). https://doi.org/10.51257/a-v1-m1191.

[2] J. Meijer, Laser beam machining (LBM), state of the art and new opportunities, Journal of Materials Processing Technology. 149 (2004) 2–17. https://doi.org/10.1016/j.jmatprotec.2004.02.003.

[3] J.F. Ready, D.F. Farson, Laser Institute of America, eds., LIA handbook of laser materials processing, Laser Institute of America ; Magnolia Pub, Orlando, FL, United States, 2001.

[4] I. Etsion, State of the Art in Laser Surface Texturing, Journal of Tribology. 127 (2005) 248–253. https://doi.org/10.1115/1.1828070.

[5] N. Mirhosseini, P.L. Crouse, M.J.J. Schmidth, L. Li, D. Garrod, Laser surface micro-texturing of Ti-6Al-4V substrates for improved cell integration, Applied Surface Science. 253 (2007) 7738–7743. https://doi.org/10.1016/j.apsusc.2007.02.168.

[6] J.C. Puoza, X. Hua, Q. Liu, Z. Kang, P. Zhang, Manufacturing of micro-textures on metals by nanosecond laser micromachining, Advances in Materials and Processing Technologies. 4 (2018) 86–99. https://doi.org/10.1080/2374068X.2017.1406268.

[7] Z. Yu, S. Yin, W. Zhang, X. Jiang, J. Hu, Picosecond laser texturing on titanium alloy for biomedical implants in cell proliferation and vascularization, J Biomed Mater Res. 108 (2020) 1494–1504. https://doi.org/10.1002/jbm.b.34497.

[8] H. Ogawa, S. Sasaki, A. Korenaga, K. Miyake, M. Nakano, T. Murakami, Effects of surface texture size on the tribological properties of slideways, Proceedings of the Institution of Mechanical Engineers, Part J: Journal of Engineering Tribology. 224 (2010) 885–890. https://doi.org/10.1243/13506501JET735.

[9] I. Etsion, Modeling of surface texturing in hydrodynamic lubrication, Friction. 1 (2013) 195–209. https://doi.org/10.1007/s40544-013-0018-y.

[10] J.L. Bottini, V. Kumar, S. Hammouti, D. Ruzic, C.S. Brooks, Influence of wettability due to laser-texturing on critical heat flux in vertical flow boiling, International Journal of Heat and Mass Transfer. 127 (2018) 806–817. https://doi.org/10.1016/j.ijheatmasstransfer.2018.06.113.

[11] K. Zhang, J. Deng, X. Guo, L. Sun, S. Lei, Study on the adhesion and tribological behavior of PVD TiAlN coatings with a multi-scale textured substrate surface, International Journal of Refractory Metals and Hard Materials. 72 (2018) 292–305. https://doi.org/10.1016/j.ijrmhm.2018.01.003.

[12] D. Kümmel, M. Hamann-Schroer, H. Hetzner, J. Schneider, Tribological behavior of nanosecond-laser surface textured Ti6Al4V, Wear. 422–423 (2019) 261–268. https://doi.org/10.1016/j.wear.2019.01.079.

[13] Y.E.B. Vidhya, A. Pattamatta, A. Manivannan, N.J. Vasa, Influence of fluence, beam overlap and aging on the wettability of pulsed Nd3+:YAG nanosecond laser-textured Cu and Al sheets, Applied Surface Science. 548 (2021) 149259. https://doi.org/10.1016/j.apsusc.2021.149259.

[14] Q. Wang, H. Wang, Z. Zhu, N. Xiang, Z. Wang, G. Sun, Switchable wettability control of titanium via facile nanosecond laser-based surface texturing, Surfaces and Interfaces. 24 (2021) 101122. https://doi.org/10.1016/j.surfin.2021.101122.

[15] A.F. Harris, A. Beevers, The effects of grit-blasting on surface properties for adhesion, International Journal of Adhesion and Adhesives. 19 (1999) 445–452. https://doi.org/10.1016/S0143-7496(98)00061-X.

[16] A. Lamraoui, S. Costil, C. Langlade, C. Coddet, Laser surface texturing (LST) treatment before thermal spraying: A new process to improve the substrate-coating adherence,

Surface and Coatings Technology. 205 (2010) S164–S167. https://doi.org/10.1016/j.surfcoat.2010.07.044.
[17] Y. Danlos, S. Costil, H. Liao, C. Coddet, Influence of Ti-6Al-4V and Al 2017 substrate morphology on Ni-Al coating adhesion – Impacts of laser treatments, Surface and Coatings Technology. 205 (2011) 2702–2708. https://doi.org/10.1016/j.surfcoat.2010.08.147.
[18] M. Perton, S. Costil, W. Wong, D. Poirier, E. Irissou, J.-G. Legoux, A. Blouin, S. Yue, Effect of Pulsed Laser Ablation and Continuous Laser Heating on the Adhesion and Cohesion of Cold Sprayed Ti-6Al-4V Coatings, J Therm Spray Tech. 21 (2012) 1322–1333. https://doi.org/10.1007/s11666-012-9812-8.
[19] K.L. Mittal, T. Bahners, eds., Laser surface modification and adhesion, Scrivener Publishing ; Wiley, Salem, Massachusetts : Hoboken, New Jersey, 2014.
[20] R. Kromer, S. Costil, J. Cormier, D. Courapied, L. Berthe, P. Peyre, M. Boustie, Laser surface patterning to enhance adhesion of plasma sprayed coatings, Surface and Coatings Technology. 278 (2015) 171–182. https://doi.org/10.1016/j.surfcoat.2015.07.022.
[21] X. Meng, K. Zhang, X. Guo, C. Wang, L. Sun, Preparation of micro-textures on cemented carbide substrate surface by plasma-assisted laser machining to enhance the PVD tool coatings adhesion, Journal of Materials Processing Technology. 288 (2021) 116870. https://doi.org/10.1016/j.jmatprotec.2020.116870.
[22] M. von Allmen, Laser-Beam Interactions with Materials, Springer Berlin Heidelberg, Berlin, Heidelberg, 1987. https://doi.org/10.1007/978-3-642-97007-8.
[23] J.-M. Jouvard, A. Soveja, L. Lavisse, Traitement de surface métallique induit par faisceau laser Nd:YAG Q-Switch de marquage : modélisation d'un impact laser, (2007) 6.
[24] P. Schaaf, ed., Laser Processing of Materials, Springer Berlin Heidelberg, Berlin, Heidelberg, 2010. https://doi.org/10.1007/978-3-642-13281-0.
[25] S.T. Hendow, S.A. Shakir, Structuring materials with nanosecond laser pulses, Opt. Express. 18 (2010) 10188. https://doi.org/10.1364/OE.18.010188.
[26] D. Bäuerle, Laser processing and chemistry, 4. ed, Springer, Berlin Heidelberg, 2011.
[27] K.-H. Leitz, B. Redlingshöfer, Y. Reg, A. Otto, M. Schmidt, Metal Ablation with Short and Ultrashort Laser Pulses, Physics Procedia. 12 (2011) 230–238. https://doi.org/10.1016/j.phpro.2011.03.128.
[28] Y. Cao, Ablation and plasma effects during nanosecond laser matter interaction in air and water, Ph.D., Purdue University, 2015. https://www.proquest.com/docview/1780301218/abstract/7976F277ACBB4D4EPQ/1.
[29] C. Sun, J. Min, J. Lin, H. Wan, S. Yang, S. Wang, The effect of laser ablation treatment on the chemistry, morphology and bonding strength of CFRP joints, International Journal of Adhesion and Adhesives. 84 (2018) 325–334. https://doi.org/10.1016/j.ijadhadh.2018.04.014.
[30] Z. Yan, X. Mei, W. Wang, A. Pan, Q. Lin, C. Huang, Numerical simulation on nanosecond laser ablation of titanium considering plasma shield and evaporation-affected surface thermocapillary convection, Optics Communications. 453 (2019) 124384. https://doi.org/10.1016/j.optcom.2019.124384.
[31] M. Trtica, B. Gakovic, D. Batani, T. Desai, P. Panjan, B. Radak, Surface modifications of a titanium implant by a picosecond Nd:YAG laser operating at 1064 and 532nm, Applied Surface Science. 253 (2006) 2551–2556. https://doi.org/10.1016/j.apsusc.2006.05.024.
[32] S. Costil, A. Lamraoui, C. Langlade, O. Heintz, R. Oltra, Surface modifications induced by pulsed-laser texturing – Influence of laser impact on the surface properties, Applied Surface Science. 288 (2014) 542–549. https://doi.org/10.1016/j.apsusc.2013.10.069.
[33] Y. Jee, M.F. Becker, R.M. Walser, Laser-induced damage on single-crystal metal surfaces, J. Opt. Soc. Am. B. 5 (1988) 648. https://doi.org/10.1364/JOSAB.5.000648.

[34] M.N. Libenson, G.D. Shandybina, A.L. Shakhmin, Chemical analysis of products obtained by nanosecond laser ablation, Tech. Phys. 45 (2000) 1219–1222. https://doi.org/10.1134/1.1318114.
[35] J. Barralis, L. Castex, G. Maeder, Précontraintes et traitements superficiels, (1999) 54.
[36] B.S. Yilbas, A.F.M. Arif, C. Karatas, M. Ahsan, Cemented carbide cutting tool: Laser processing and thermal stress analysis, Applied Surface Science. 253 (2007) 5544–5552. https://doi.org/10.1016/j.apsusc.2006.12.123.
[37] L. Van Belle, Analyse, modélisation et simulation de l'apparition de contraintes en fusion laser métallique, INSA de Lyon, 2013. https://tel.archives-ouvertes.fr/tel-01153233/document.
[38] M.V. Zhidkov, N.A. Smirnov, J. Chen, S.I. Kudryashov, I.Y. Goncharov, Residual stresses in Ti6Al4V alloy after surface texturing by femtosecond laser pulses, IOP Conf. Ser.: Mater. Sci. Eng. 862 (2020) 022060. https://doi.org/10.1088/1757-899X/862/2/022060.
[39] E. Maawad, Y. Sano, L. Wagner, H.-G. Brokmeier, Ch. Genzel, Investigation of laser shock peening effects on residual stress state and fatigue performance of titanium alloys, Materials Science and Engineering: A. 536 (2012) 82–91. https://doi.org/10.1016/j.msea.2011.12.072.
[40] K. Gurusami, D. Chandramohan, S. Dinesh Kumar, M. Dhanashekar, T. Sathish, Strengthening mechanism of Nd: Yag laser shock peening for commercially pure titanium (CP-TI) on surface integrity and residual stresses, Materials Today: Proceedings. 21 (2020) 981–987. https://doi.org/10.1016/j.matpr.2019.09.141.
[41] A.E. Siegman, Lasers, Univ. Science books, Mill Valley, Calif, 1986.
[42] V. Semak, A. Matsunawa, The role of recoil pressure in energy balance during laser materials processing, J. Phys. D: Appl. Phys. 30 (1997) 2541–2552. https://doi.org/10.1088/0022-3727/30/18/008.
[43] C. Zhang, J. Zhou, H. Shen, Role of Capillary and Thermocapillary Forces in Laser Polishing of Metals, Journal of Manufacturing Science and Engineering. 139 (2017) 041019. https://doi.org/10.1115/1.4035468.
[44] N. Fairley, V. Fernandez, M. Richard-Plouet, C. Guillot-Deudon, J. Walton, E. Smith, D. Flahaut, M. Greiner, M. Biesinger, S. Tougaard, D. Morgan, J. Baltrusaitis, Systematic and collaborative approach to problem solving using X-ray photoelectron spectroscopy, Applied Surface Science Advances. 5 (2021) 100112. https://doi.org/10.1016/j.apsadv.2021.100112.
[45] V. Hauk, H. Behnken, Structural and residual stress analysis by nondestructive methods evaluation, application, assessment, Elsevier, Amsterdam; New York, 1997. http://www.123library.org/book_details/?id=38904.
[46] W.A. Rachinger, A Correction for the α1 α2 Doublet in the Measurement of Widths of X-ray Diffraction Lines, J. Sci. Instrum. 25 (1948) 254–255. https://doi.org/10.1088/0950-7671/25/7/125.
[47] Keysight Technologies, Data Sheet, Scanning Microwave Microscopy (SMM) Mode, (2014). https://www.keysight.com/us/en/assets/7018-01857/data-sheets/5989-8817.pdf.
[48] Agilent Technologies, Data Sheet, 5600LS AFM, (n.d.). https://www.agilent.com/cs/library/datasheets/public/5600LS_5989-8819.pdf.
[49] Copper Mountain Technologies, Data Sheet, R180 VNA, (n.d.). https://coppermountaintech.com/wp-content/uploads/2018/11/R180-Extended-Specification-Sheet.pdf.
[50] Rocky Mountain Nanotechnology, Data Sheet, 12PT400B probe, (n.d.). https://rmnano.com/tech-data.

[51] C. Plassard, E. Bourillot, J. Rossignol, Y. Lacroute, E. Lepleux, L. Pacheco, E. Lesniewska, Detection of defects buried in metallic samples by scanning microwave microscopy, Phys. Rev. B. 83 (2011) 121409. https://doi.org/10.1103/PhysRevB.83.121409.
[52] Granta Design Limited, CES Selector software, Cambridge, UK, 2014. www.grantadesign.com.
[53] P. Vitry, Applications and development of acoustic and microwave atomic force microscopy for high resolution tomography analysis, Université de Bourgogne, 2016. https://tel.archives-ouvertes.fr/tel-01635664/document.